ACS APPLIED MATERIALS & INTERFACES

www.acsami.org

Research Article

Native Atomic Defects Manipulation for Enhancing the Electronic Transport Properties of Epitaxial SnTe Films

Fuqiang Hua,† Pengfei Lv,† Min Hong, Sen Xie, Min Zhang, Cheng Zhang, Wei Wang, Zhaohui Wang, Yong Liu, Yonggao Yan, Shengjun Yuan, Wei Liu,* and Xinfeng Tang*

Cite This: https://doi.org/10.1021/acsami.1c15447

Read Online

ACCESS | Metrics & More | Article Recommendations | Supporting Information

ABSTRACT: P-type SnTe-based compounds have attracted extensive attention because of their high thermoelectric performance. Previous studies have made tremendous efforts to investigate native atomic defects in SnTe-based compounds, but there has been no direct experimental evidence so far. On the basis of MBE, STM, ARPES, DFT calculations, and transport measurements, this work directly visualizes the dominant native atomic defects and clarifies an alternative optimization mechanism of electronic transport properties via defect engineering in epitaxially grown SnTe (111) films. Our findings prove that positively charged Sn vacancies (V_{Sn}) and negatively charged Sn interstitials (Sn_i) are the leading native atomic defects that dominate electronic transport in SnTe, in contrast to previous studies that only considered V_{Sn}. Increasing the substrate temperature (T_{sub}) and decreasing the Te/Sn flux ratio during film growth reduces the density of V_{Sn} while increasing the density of Sn_i. A high T_{sub} results in a low hole density and high carrier mobility in SnTe films. The SnTe film grown at T_{sub} = 593 K and Te/Sn = 2/1 achieves its highest power factor of 1.73 mW m^{-1} K^{-2} at 673 K, which is attributed to the optimized hole density of 2.27 × 10^{20} cm^{-3} and the increased carrier mobility of 85.6 cm^2 V^{-1} s^{-1}. Our experimental studies on the manipulation of native atomic defects can contribute to an increased understanding of the electronic transport properties of SnTe-based compounds.

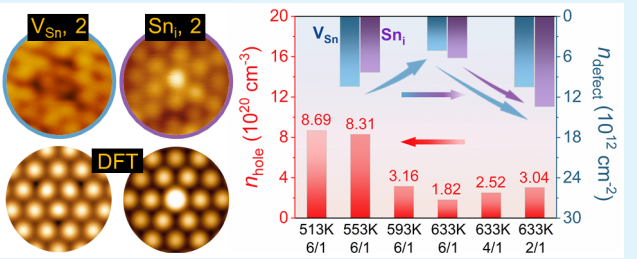

KEYWORDS: *SnTe films, MBE, STM, ARPES, native atomic defects, electronic transport properties*

1. INTRODUCTION

Thermoelectric (TE) materials enable the direct conversion between heat and electricity based on the Seebeck and Peltier effects, and have promising applications in fields such as waste heat recovery, self-powered wearable devices, heat dissipation for electronic devices, and radioisotope power generators for deep-space exploration.[1−5] The conversion efficiency of TE devices is determined by the dimensionless figure of merit (ZT) of TE materials, $ZT = \sigma S^2 T/(\kappa_e + \kappa_L)$, where σ, S, κ_e, κ_L, and T signify the electrical conductivity, Seebeck coefficient, electronic thermal conductivity, lattice thermal conductivity, and absolute temperature, respectively.[6] Enhancing the power factor (PF = σS^2) and decreasing the total thermal conductivity ($\kappa_e + \kappa_L$) are the main ways to improve ZT.

P-type SnTe-based materials have sparked broad interest because of their excellent TE performances, and they are well-known as eco-friendly alternatives to PbTe that are free of toxic elements.[7] The combination of band structure engineering[8] and phonon engineering[9] has been demonstrated to effectively increase the ZT values of SnTe, with the maximum ZT increasing from approximately 0.6 in pristine SnTe to approximately 1.8 in nanostructured SnTe based alloys.[10−12] Alloying Mn, Mg, Cd, and Hg[13−16] in SnTe effectively reduced the energy offset between the light valence band (L) and the heavy valence band (Σ), and broadened the energy band gap, leading to significantly increased ZT values. Moreover, In doping was reported to produce resonant energy levels near the Fermi level (E_F) in the density of states of SnTe, resulting in increased S.[17,18] For phonon engineering in SnTe, introducing atomic defects,[12,19,20] dislocations,[21] and nanostructures[11,22] was confirmed to scatter phonons over a wide-frequency range. Therefore, κ_L was reduced toward its amorphous limit of 0.4 W m^{-1} K^{-1}, as determined by the Debye−Cahill model.[20,23]

Prior to implementing the strategies mentioned above, the hole density should be optimized to maximize the ZT of p-type SnTe. This is because the p-type SnTe has an excessively large hole density of approximately 1 × 10^{21} cm^{-3}, which results from the high density of native Sn vacancies (V_{Sn}).[24,25] Consequently, the PF deteriorates and the κ_e increases, both of which significantly reduce the ZT of SnTe. To reduce the hole

Received: August 13, 2021
Accepted: November 3, 2021

density of SnTe, researchers have used the counter-doping of Bi,[26−28] Sb,[24,28] Gd,[24,29] and excess Sn[28,30] on the cation sites as well as I doping on the anion sites.[31,32] Among these dopants, only Bi and I reduce the hole density to the optimal range of approximately 4×10^{19} cm^{-3}, which is mainly influenced by V_{Sn} because of its lowest formation energy among all types of defects.[33] Despite the optimized hole density obtained by doping, the associated point defects deteriorate the carrier mobility and thus the power factor to some extent.[34] Therefore, suppressing the high-density V_{Sn} to optimize the hole density is expected to achieve better TE performance in SnTe-based alloys than doping would. However, the mechanism of controlling V_{Sn} has not yet been thoroughly investigated. Moreover, to further improve the electronic properties, other types of native atomic defects should be thoroughly investigated experimentally in SnTe.

Combinations of molecular beam epitaxy (MBE), scanning tunneling microscopy (STM), and angle-resolved photoemission spectroscopy (ARPES) are effective in uncovering the atomic defects and their important features, which was recently demonstrated in the Bi_2Te_3-based TE films.[35,36] Although some preliminary results have been reported in SnTe materials by using STM, atomic defects have never been investigated systematically.[37,38] Thus, using the combined techniques of MBE-STM-ARPES and transport property measurements, this work thoroughly examines native atomic defects and their influence on the electronic transport properties of SnTe (111) films. Guided by these findings, the hole density is optimized, and the electrical properties are remarkably improved by the manipulating atomic defects in the as-grown SnTe (111) films. This study provides an innovative method for enhancing the TE performances of SnTe and other broad material systems by engineering atomic defects.

2. EXPERIMENTAL PROCEDURES

Film Growth and the Characterization of Atomic Defects. The SnTe (111) single-crystalline films were epitaxially grown by the molecular beam epitaxy apparatus (MBE, Octoplus 300, Dr. Eberl MBE Komponenten). We utilized a 6 nm thick Bi_2Te_3 (00*l*) film fabricated on a sapphire (00*l*) substrate as the buffer layer. High-purity Bi (99.999%) and Sn (99.9999%) were evaporated from standard Knudsen cells, and high-purity Te (99.9999%) was evaporated from a special two-stage thermal cracker cell. The fluxes of Bi, Sn and Te were monitored in situ with a quartz crystal oscillator. The fluxes of Bi and Sn were held constant at 0.025 and 0.04 Å/s for Bi_2Te_3 and SnTe, respectively. The Te to Bi flux ratio (Te/Bi) was set to 6/1 and the substrate temperature (T_{sub}) was set to 573 K during the growth of Bi_2Te_3. The Te to Sn flux ratio (Te/Sn) and T_{sub} were set in the ranges of 2/1−18/1 and 513−633 K, respectively, during the growth of SnTe. The growth rates of the Bi_2Te_3 buffer layers and SnTe films were calibrated at approximately 0.3 and 0.4 nm/min, respectively, to ensure high crystallinity. In situ reflection high-energy electron diffraction (RHEED) was used to monitor the growth process in real time.

Surface morphologies and atomic defects were characterized in situ with a low-temperature scanning tunneling microscope (LT-STM-AFM-N, CreaTec Fisher & Co. GmbH) at the LN_2 temperature. The surface electronic band structures were characterized in situ at 10 K using an angle-resolved photoemission spectroscopy system (ARPES, Scienta Omicron). A monochromatic He−I ($h\nu$ = 21.2 eV) light source and a state-of-the-art DA-30L hemispherical electron analyzer were used during the ARPES measurements. High energy and angle resolutions of 7 mV and 0.2°, respectively, ensured accurate characterization of electronic structures of SnTe films. The STM and ARPES apparatuses were interconnected with the MBE growth chamber by a UHV transfer tunnel. The phase structure of the as-grown SnTe films was examined by high-resolution X-ray diffraction measurements (HRXRD, Rigaku Smartlab), including $\theta-2\theta$ scans and φ scans.

Electronic Property Characterizations. The Seebeck coefficient and the electrical conductivity of SnTe films were measured simultaneously on CTA-3 equipment in a helium atmosphere and at temperatures ranging from room temperature to 673 K. The Hall coefficient (R_H) at room temperature was measured by using a five-point configuration in a physical property measurement system (PPMS-9T, Quantum Design). The room-temperature hole density (p) and carrier mobility (μ) were calculated based on the equations $p = 1/eR_H$ and $\mu = R_H\sigma$. We measured the thicknesses of the as-grown films with a step profiler (DektakXT, Bruker). The surface area of the measured films was approximately 10 mm × 3 mm for CTA-3 and PPMS measurements. The uncertainties of the Seebeck coefficient, electrical conductivity and Hall coefficient measurements were ±5%, ± 10% and ±5%, respectively.

DFT Calculations Regarding Native Atomic Defects. Formation energy (E_{form}) calculations were performed using QUANTUM-ESPRESSO.[39] The exchange and correlation interactions were described using the Perdew−Burke−Ernzerhof (PBE).[40] Values of 100 and 400 Ry were chosen as the cut-offs for the selection of the plane-wave basis sets to describe the kinetic energy and the electronic density, respectively. The spin−orbit coupling effect (SOC) was considered in the calculations. A supercell of 3 × 3 × 3 $Sn_{27}Te_{27}$ built from the primitive cell was used in the calculation. The structure was fully relaxed when the total energy changed to less than 1×10^{-5} eV between two consecutive self-consistent calculations and all components of all forces were smaller than 10^{-4} eV/ Å. E_{form} was calculated from the equation $E_{form} = E_{tot}(X^q) - E_{tot}(\text{host}) - \Sigma n_i\mu_i + q(E_F + E_v + \Delta V)$, where $E_{tot}(X^q)$ and $E_{tot}(\text{host})$ are the total energies of the supercells with and without defects, respectively.[41] n_i is the number of type i atoms that are added to ($n_i > 0$) or removed from ($n_i < 0$) the supercell when the defect is created, and u_i is the corresponding chemical potential. μ_{Sn} and μ_{Te} are calculated by $\mu_{Sn} + \mu_{Te} = E_{SnTe}$, where E_{SnTe} represents the cohesive energy of SnTe. In the Sn-rich condition, u_{Sn} equaled the cohesive energy of Sn (E_{Sn}), whereas in the Te-rich condition, u_{Te} equaled the cohesive energy of Te (E_{Te}). The E_{Sn} and E_{Te} are calculated based on the diamond cubic phase of Sn and the trigonal phase of Te, respectively. q is the charge value of the defect. E_F is the Fermi level with respect to the valence band maximum (E_v). ΔV is a correction term used to align the reference electrostatic potential in the defect supercell with that in the perfect bulk.

The STM simulations of the SnTe surface atomic defects were performed using the projector augmented wave (PAW) method,[42] which was implemented in the *Vienna Ab initio Simulation Package* (VASP) code.[43] We used the PBE parametrization[40] of the generalized gradient approximation to express the exchange-correlation function, and the atomic core electron interactions were represented by the PAW pseudopotential.[42] To model the surface structure and potential atomic defects of SnTe, which consists of four atomic layers along the (111) direction (Te1−Sn1−Te2−Sn2, referred to as quadruple layers (QLs)), we used the supercell approach without considering the SOC effect. We chose the (4 × 4) surface unit cells consisting of two QLs and added a 20 Å vacuum slab to avoid spurious interactions. The structure was relaxed using conjugate gradient (CG) geometry optimization until the residual force on each atom was less than 0.01 eV/Å. A Monkhorst−Pack scheme[44] k-point grid of 5 × 5 × 1 was used for the structural relaxation and a grid of 7 × 7 × 1 was used for self-consistent field calculations until the change in total energy was less than 1×10^{-5} eV. The simulated STM images were generated by using the Tersoff−Hamann approximation[45,46] at a distance approximately 2 Å above the surface.

https://doi.org/10.1021/acsami.1c15447
ACS Appl. Mater. Interfaces XXXX, XXX, XXX−XXX

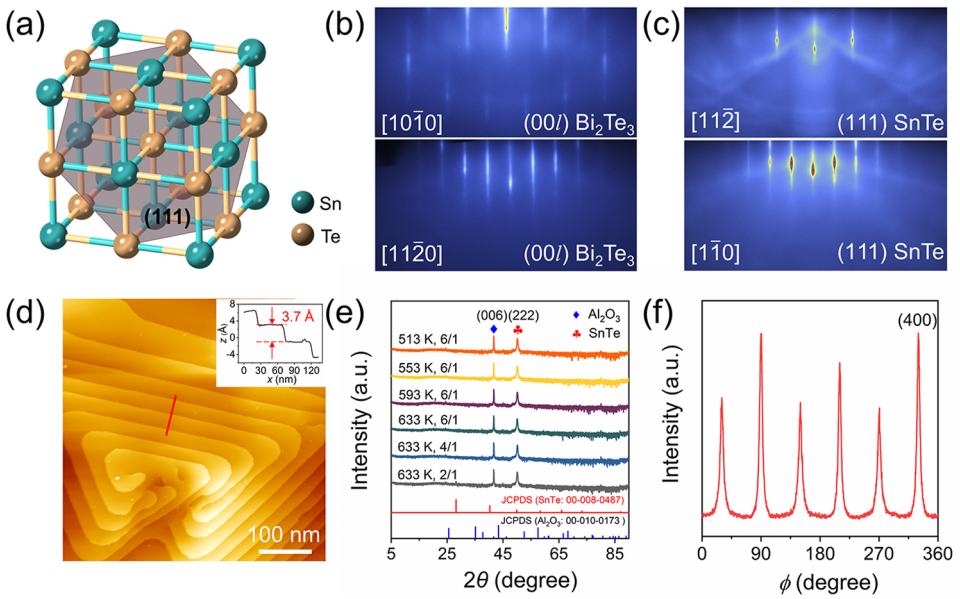

Figure 1. (a) Crystal structure of cubic SnTe. The purple shadow represents the (111) lattice plane of SnTe. RHEED patterns of the (b) Bi_2Te_3(00l) buffer layer along the [10$\bar{1}$0] and [11$\bar{2}$0] azimuthal directions and (c) SnTe (111) film grown at T_{sub} = 633 K and Te/Sn = 6/1 along the [11$\bar{2}$] and [1$\bar{1}$0] azimuthal directions. (d) In situ STM surface morphology of the as-grown SnTe film, showing triangular-shaped terraces and spirals. (e) XRD spectra of θ–2θ for SnTe films grown at various T_{sub} and Te/Sn ratios. (f) XRD spectrum of the φ-scan for the SnTe film grown at T_{sub} = 633 K and Te/Sn = 6/1. The inset in d illustrates the step height of SnTe, marked by the red line, which represents the stacking units of −Sn−Te− with a thickness of 3.7 Å.

3. RESULTS AND DISCUSSION

3.1. Phase Structure and Surface Morphology. SnTe crystallizes in a rock salt crystal structure with hexagonal Sn and Te sublattices stacking along the [111] crystallographic direction, as displayed in Figure 1a. The purple shadow represents the (111) lattice plane of SnTe. The lattice-match between the substrate and the product is required for the epitaxial growth of high-quality films. The rhombohedral Bi_2Te_3 (00l) buffer layer, with a surface lattice mismatch of ∼1.5% with respect to SnTe (111), satisfies this requirement.[47] Figure 1b, c exhibit the RHEED patterns of the fabricated Bi_2Te_3 buffer layer and the SnTe film epitaxially grown on a sapphire (Al_2O_3) substrate. The growth of the Bi_2Te_3 buffer layer is similar to that of the reference,[48] and the buffer layer has a highly crystalline quality. The outermost Te atomic layer of the Bi_2Te_3 buffer layer can naturally accommodate the Te or Sn atomic layer of SnTe (111), resulting in the high-quality epitaxial growth of SnTe (111) films, as evidenced by sharp RHEED streaks and clear Kikuchi lines. Figure 1d shows the STM surface morphology of the epitaxial SnTe (111) film. The surface of the SnTe (111) film is characterized by triangular islands and spirals with atomic flat terraces, indicating that the layer growth mode of SnTe on the Bi_2Te_3 buffer layer is consistent with the reported results.[47] At the expense of surface energy, the formation of triangle islands and spirals structures could reduce epitaxial lattice strain during the layer-by-layer growth of SnTe. Furthermore, the step height of 3.7 Å along the red line agrees well with the thickness of the periodic unit of −Sn−Te− along the [111] direction, corroborating the sequential stacking of Sn and Te layers as well as the layer growth mode. As shown in Figure 1e, the SnTe (111) films grown at various T_{sub} and Te/Sn ratios exclusively have the (222) diffraction peak, with the exception of the (006) peak from the sapphire substrate, indicating that the epitaxial SnTe films all have single-crystal characteristics. Furthermore, the HRXRD φ-scan in Figure 1f demonstrates a 3-fold symmetry of the {400} planes along the [111] direction as well as a prominent twin structure in the as-grown SnTe (111) film. The 3-fold symmetry is revealed by two sets of peaks with equivalent intensities that appear at 30, 150, and 270° as well as at 90, 210, and 330°. The twin structure in the SnTe film is inherited from the Bi_2Te_3 buffer layer, which tends to have a twin structure when grown on sapphire substrates.[49]

3.2. Atomic Defect Structure. Figure 2 depicts the calculated formation energies (E_{form}) of all possible atomic defects in SnTe under Sn-rich and Te-rich environments using DFT calculations. Sn vacancies (V_{Sn}) are the dominant atomic defects in SnTe because they have the lowest E_{form} among the various atomic defects, which well supports the highly degenerated p-type conduction in SnTe.[25,50] In addition to V_{Sn}, other atomic defects with relatively high E_{form} can also exist under different growth environments. Antisite defects of Sn_{Te} and Te_{Sn} are likely to form in Sn-rich and Te-rich

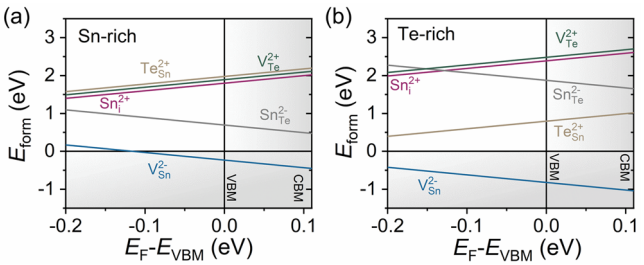

Figure 2. Calculated formation energies (E_{form}) of possible defects in SnTe under (a) Sn-rich and (b) Te-rich environments as a function of $E_F - E_{VBM}$ with E_F and E_{VBM} denoting the Fermi level and valence band maximum, respectively. The slope of the line indicates the charge state of the defect. The E_F ranges from 0.2 eV below the valence band maximum to the conduction band minimum.

https://doi.org/10.1021/acsami.1c15447
ACS Appl. Mater. Interfaces XXXX, XXX, XXX−XXX

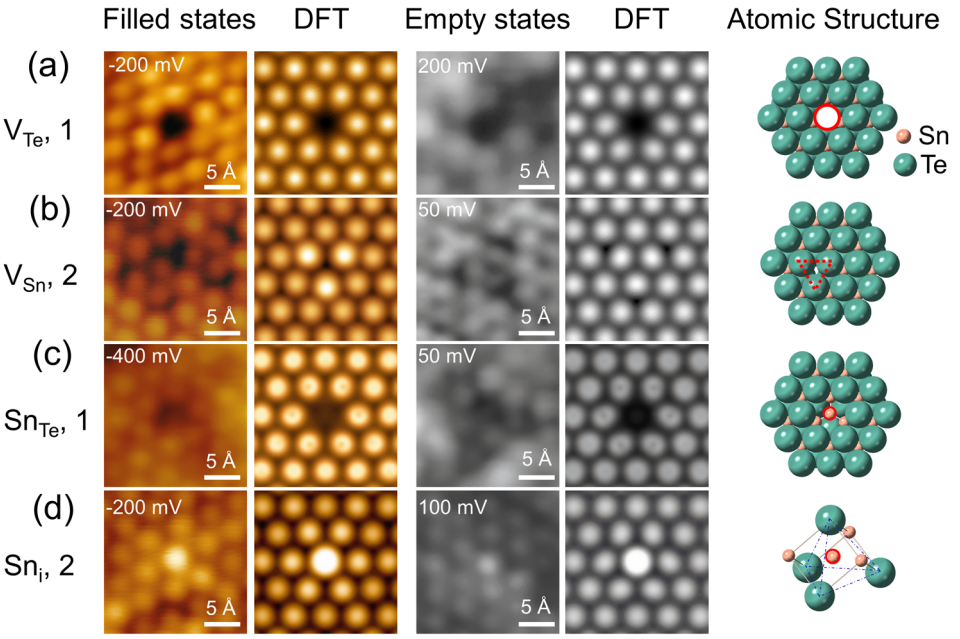

Figure 3. STM tip bias-dependent surface topographies of atomic defects in SnTe (111) films: (a) Te vacancies (V_{Te}, 1) and (c) Sn antisites (Sn_{Te}, 1) at the first atomic layer as well as (b) Sn vacancies (V_{Sn}, 2) and (d) interstitial Sn (Sn_i, 2) at the second atomic layer in filled states and empty states. The experimental and DFT-simulated STM characteristic topographies and the schematic atomic structures are listed for these defects. The experimental results are made consistent with the DFT simulated STM topographies by assuming that the outermost terminated surface is the Te atomic layer. The numbers 1 and 2 represent the atomic defects at the outermost Te layer and the underneath layer, respectively.

environments, respectively, because of their low E_{form} of less than 1.0 eV. Sn_{Te} and Te_{Sn} function as electron acceptors and electron donors, respectively. In addition, donor-like interstitial defects Sn_i, located in the tetrahedral interstice of Te atoms, may exist in the Sn-rich environment due to the relatively low E_{form}. Therefore, in addition to the V_{Sn}, other types of atomic defects such as Sn_{Te}, Te_{Sn}, and Sn_i can exist in SnTe and hence influence the electronic transport properties.

Intuitively, the types of various atomic defects can be identified based on the STM surface morphologies and DFT simulations. For example, vacancies exhibit dark depression characteristics in the STM topography, because the STM image contrast is very sensitive to the surface height.[36] Figure 3 and Figure S1 show the tip bias-dependent STM topographies used to examine surface atomic defects in SnTe films. Wang et al.[51] calculated the stability of the SnTe (111) surface and found that the stably terminated surface was either the Te (111) or the reconstructed Sn-terminated surface that diminishes the surface energy. Experimentally, we confirmed that the terminated surface of the SnTe films is Te (111). First, there was no surface reconstruction in the atomically resolved STM images of the SnTe films. Second, the STM topographies and DFT simulations of surface atomic defects are consistent, further confirming that Te (111) is the stably terminated surface. In the STM topographies, the V_{Te} at the terminated Te layer corresponds to the dark hole in both the filled states (negative bias) and empty states (positive bias). The V_{Sn} at the second atomic layer has a trigonal shape in STM topographies with dark depression characteristics in both the filled states and empty states, because of he 3-fold symmetry of the crystal lattice along the [111] direction and the local lattice distortion caused by the V_{Sn}. Because the ionic radius of Sn^{2+} (0.93 Å) is much smaller than that of Te^{2-} (2.21 Å), the STM topographies of antisite Sn_{Te} at the first atomic layer show dark depressions. Furthermore, interstitial Sn_i exhibit bright protrusions in the STM images. Our in situ STM studies reveal the existence of positively charged V_{Sn} and Sn_{Te} as well as negatively charged V_{Te} and Sn_i, which are believed to be native atomic defects in the SnTe (111) films, whereas other defects are not prominent in the films.

It was reported that the MBE growth parameters significantly impacted the atomic defects in Bi_2Te_3 films.[36] A similar phenomenon was found in SnTe films. Figure 4 shows the STM surface morphologies and the quantitative analysis of atomic defects in SnTe (111) films grown at various T_{sub} and Te/Sn ratios. All SnTe films exhibited native atomic defects of V_{Sn}, Sn_i, Sn_{Te}, and V_{Te}, which are well distinguished by their characteristic STM morphologies, as labeled in Figure 4a–c. The densities of V_{Sn} and Sn_i are greater than those of the other two types of defects, indicating that V_{Sn} and Sn_i are the main defects in the SnTe films. As shown in Figure 4d, the statistical analysis of atomic defects from samples grown at different conditions has revealed that both T_{sub} and Te/Sn impact the densities of V_{Sn} and Sn_i. First, as T_{sub} increases from 553 to 633 K, the sheet density of V_{Sn} reduces dramatically from 1.04×10^{13} cm^{-2} to 5.08×10^{12} cm^{-2}. Arising from the volatility of element Te, increasing T_{sub} reduces the Te content in SnTe films, which increases the actual Sn content and decreases the V_{Sn} density. Second, reducing the Te/Sn flux ratio at elevated T_{sub} = 633 K increases the sheet densities of V_{Sn} and Sn_i from 5.08×10^{12} cm^{-2} and 6.25×10^{12} cm^{-2} at Te/Sn = 6/1 to 1.05×10^{13} cm^{-2} and 1.35×10^{13} cm^{-2} at Te/Sn = 2/1, respectively. Previous studies reported by Xin et al.[20] suggested that introducing n-type V-interstitial defects decreased E_{form} and increased the density of native V_{Sn}. In our research, excess Sn and high T_{sub} promote the formation of energetically unfavorable Sn_i, leading to a higher density of V_{Sn}, originating from the n–p compensation doping of positively charged V_{Sn}

https://doi.org/10.1021/acsami.1c15447
ACS Appl. Mater. Interfaces XXXX, XXX, XXX–XXX

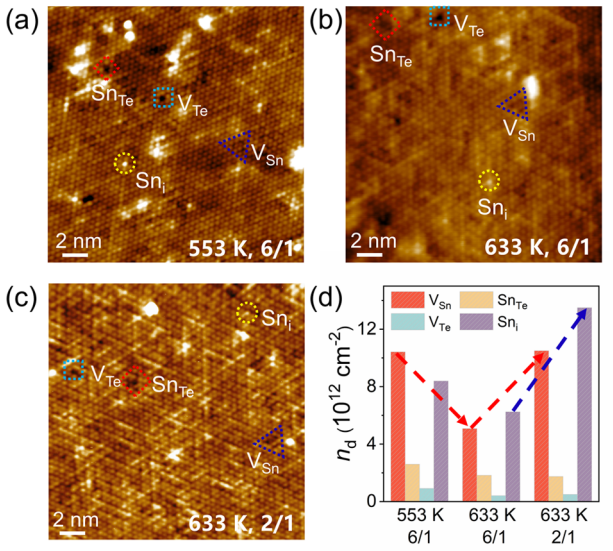

Figure 4. Atomically resolved STM surface morphologies (20 nm × 20 nm) of SnTe (111) films grown at different conditions of (a) T_{sub} = 553 K and Te/Sn = 6/1, (b) T_{sub} = 633 K and Te/Sn = 6/1, and (c) T_{sub} = 633 K and Te/Sn = 2/1. (d) Statistical analysis of the sheet densities of atomic defects for SnTe films grown at different growth parameters.

and negatively charged Sn_i. Based on the evolution of the atomic defects at different MBE growth parameters, two regulation mechanisms for V_{Sn} and Sn_i are summarized. For V_{Sn}, the lowest E_{form} among all atomic defects urges the formation of a large amount of V_{Sn} under Te-rich or even Sn-rich conditions, which is described by the following equation:

$$\mathrm{Sn} + \mathrm{Te} = (1 - x)\mathrm{Sn_{Sn}} + \mathrm{Te_{Te}} + x\mathrm{Sn} + x\mathrm{V_{Sn}^{''}} + 2x\mathrm{h^{\cdot}} \quad (1)$$

where the excess Sn may transform into p-type Sn_{Te} defects or result in the formation of Sn-rich precipitates. Moreover, under Sn-rich and high thermal energy conditions, the formation of high-density V_{Sn} and Sn_i can be illustrated as follows:

$$\mathrm{Te} + (1 + x)\mathrm{Sn} \rightarrow \mathrm{Te_{Te}} + (1 - y)\mathrm{Sn_{Sn}} + x\mathrm{Sn_i^{z+}} + y\mathrm{Sn} + y\mathrm{V_{Sn}^{''}} + (2y - zx)\mathrm{h^{\cdot}} \quad (2)$$

Unlike previous reports that focused solely on V_{Sn} as the predominating atomic defect, this work concludes that V_{Sn} and Sn_i are both major defects in SnTe. As shown in Figure 4d, the sheet density of n-type Sn_i is comparable to that of p-type V_{Sn}, whereas all SnTe films are highly degenerated p-type semiconductors with high hole densities. This implies that the density of Sn_i in the interior film is reduced because of the evolution of defects induced by a continuously heated substrate during the film growth process.

3.3. Electronic Transport Manipulated by Atomic Defects. ARPES and Hall measurements are effective in clarifying the effects of atomic defects on electronic transport in SnTe. Figure 5 shows the ARPES surface electronic structures and the corresponding MDC spectra along the $\bar{\Gamma}$–$\bar{K}$ direction at 10 K of the as-grown SnTe (111) films. SnTe is a direct band gap semiconductor with both the valence band maximum (VBM) and the conduction band minimum (CBM) at the high-symmetry L point in the bulk Brillouin zone (BZ).[52] The VBM is projected to the $\bar{\Gamma}$ point of the surface BZ along the [111] direction, as depicted in Figure S2. Because of the strong p-type conduction of SnTe films, the VBM is not observed in our ARPES results. Instead, we use valence band 2 (VB2) as a reference to display the movement of E_F. The E_F from the ARPES measurements shifts upward as T_{sub} increases from 513 to 633 K in SnTe films, coinciding with the decreased density of positively charged V_{Sn} and p, as shown in Figure 4 and Table 1. Specifically, E_F shows an upshift by approximately 0.2 eV, and p decreases from 8.69 × 10^{20} cm^{-3} to 1.82 × 10^{20} cm^{-3}. Additionally, in SnTe films grown at T_{sub} of 633 K, a decrease in the Te/Sn ratio from 6/1 to 2/1 results in a slight downshift in E_F and a moderate increase in p, from

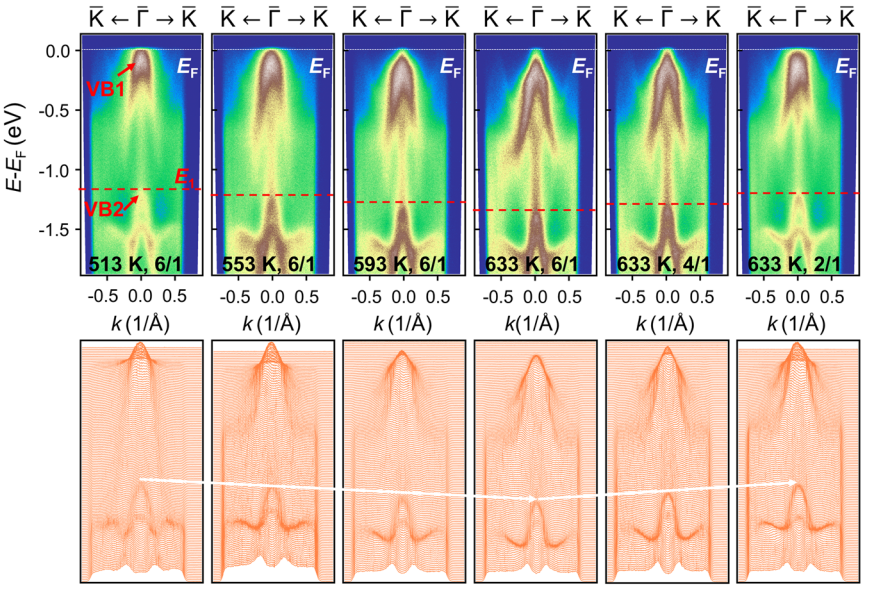

Figure 5. In situ ARPES surface electronic structures (upper panels) and the corresponding momentum distribution curves (MDCs) spectra (lower panels) along the $\bar{\Gamma}$–$\bar{K}$ direction at 10 K for SnTe (111) films grown at various T_{sub} and Te/Sn ratios. VB1 and VB2 represent bulk valence bands 1 and 2, respectively, as indicated by the red arrows. E_F is the Fermi level and E_1 is the energy position of bulk valence band 2.

https://doi.org/10.1021/acsami.1c15447
ACS Appl. Mater. Interfaces XXXX, XXX, XXX–XXX

Table 1. Room-Temperature Physical Parameters of SnTe (111) Films Grown at Various T_{sub} and Te/Sn Ratios, Including Hole Density (p), Carrier Mobility (μ), Electrical Conductivity (σ), Seebeck Coefficient (S), and Power Factor (PF)

T_{sub} (K)	Te/Sn	p ($\times 10^{20}$ cm^{-3})	μ (cm^2 V^{-1} s^{-1})	σ ($\times 10^4$ S m^{-1})	S (μV K^{-1})	PF (mW m^{-1} K^{-2})
513	6/1	8.69	24.6	34.2	44	0.67
553	6/1	8.31	28.8	38.4	51	1.01
593	6/1	3.16	65.7	33.3	49	0.80
633	6/1	1.82	74.5	21.7	42	0.38
593	2/1	2.27	85.6	31.1	42	0.54
593	10/1	2.64	48.9	20.6	34	0.23
593	14/1	2.83	45.4	20.6	48	0.46
593	18/1	2.96	33.5	15.9	50	0.40
633	2/1	3.04	86.7	42.2	39	0.69
633	4/1	2.52	70.2	28.3	42	0.51

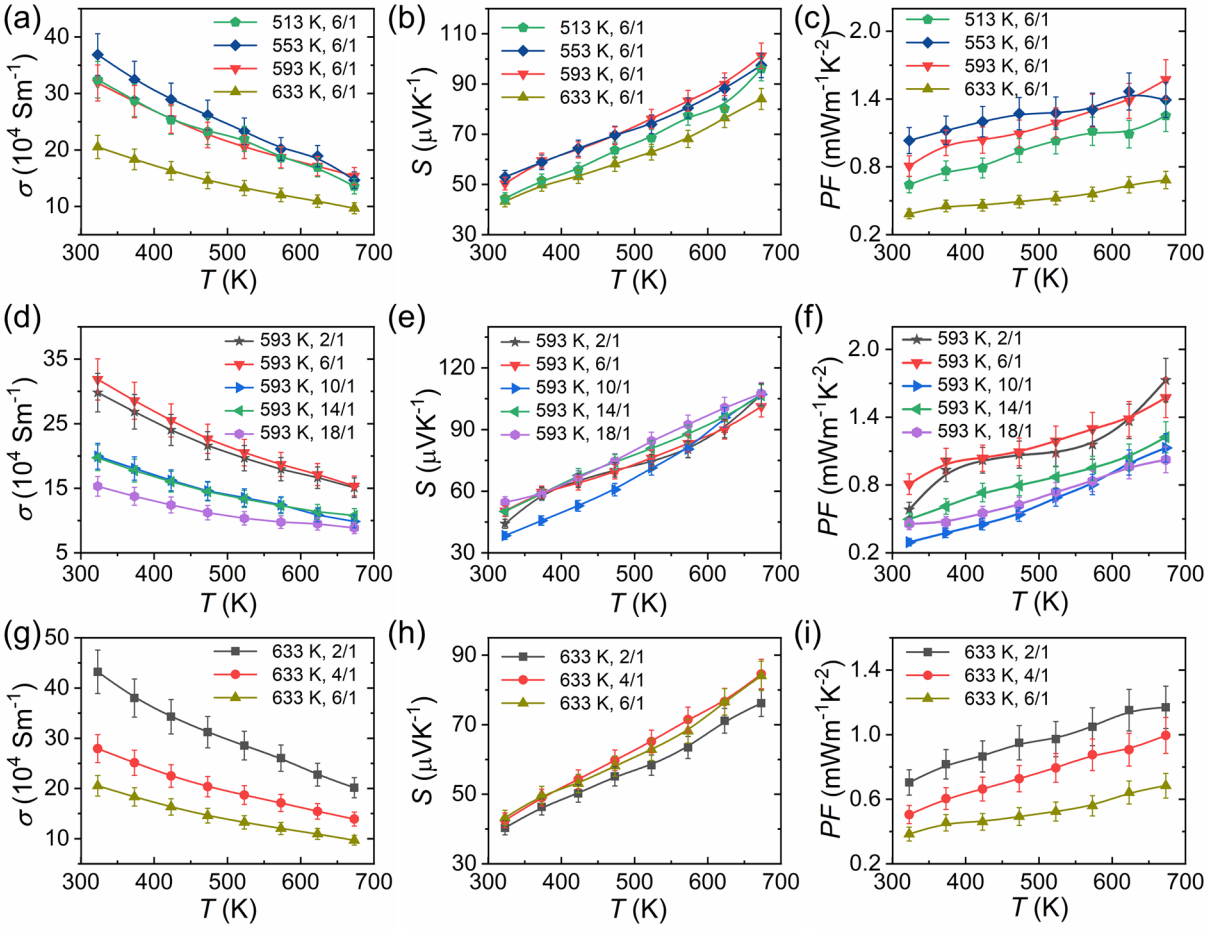

Figure 6. Temperature dependence of the electrical conductivity, Seebeck coefficient, and power factor for the SnTe (111) films: (a–c) Te/Sn = 6/1 and various T_{sub}; (d–f) T_{sub} = 593 K and various Te/Sn; (g–i) T_{sub} = 633 K and various Te/Sn.

1.82×10^{20} cm^{-3} to 3.04×10^{20} cm^{-3}. It should be noted that the variation trends of p and E_F are not clear in SnTe films grown at T_{sub}= 593 K with Te/Sn ratios ranging from 18/1 to 2/1, as shown in Figure S3 and Table 1. This result suggests that both the positively charged V_{Sn} and negatively charged Sn_i are sensitive to the MBE growth parameters, leading to fluctuations in electronic transport in SnTe films. Furthermore, we discover that T_{sub} and the Te/Sn ratio also play an important role in tuning the carrier mobility (μ) of SnTe films, as listed in Table 1. Increasing T_{sub} increases μ because of the improved crystallinity of the films, whereas increasing the Te/Sn ratio decreases μ, which is caused by the film growth deviating from the optimal condition. The highest μ of approximately 80 cm^2 V^{-1} s^{-1} in SnTe films is obtained when the T_{sub} is 593 or 633 K and the Te/Sn ratio is 2/1, which is more than double that obtained in the film grown when T_{sub} is 513 K and the Te/Sn ratio is 6/1.

Figure 6 depicts the temperature-dependent electrical transport properties of SnTe (111) films grown at different conditions. In all SnTe films, the room-temperature electrical conductivity (σ) is larger than 15×10^4 S m^{-1}, and the Seebeck coefficient (S) increases monotonically with temperature. Over the temperature range studied, all samples contain completely different σ but roughly similar S. Thus, the PF

https://doi.org/10.1021/acsami.1c15447
ACS Appl. Mater. Interfaces XXXX, XXX, XXX−XXX

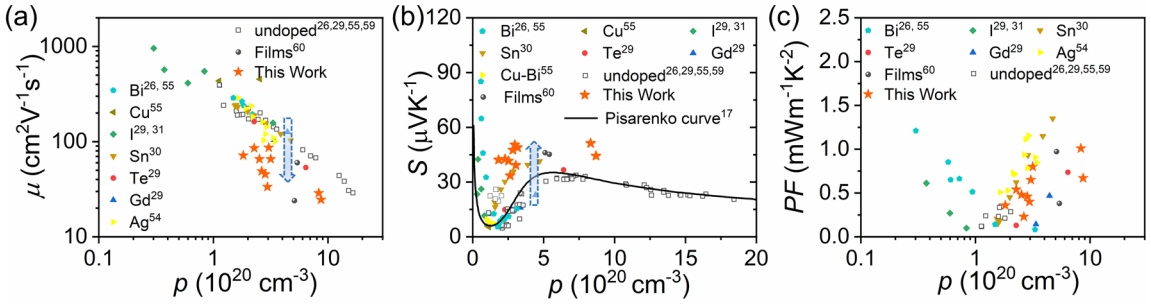

Figure 7. Carrier density dependence of the (a) carrier mobility, (b) Seebeck coefficient, and (c) power factor for SnTe films at room temperature, and a comparison with reported results. The black line in b indicates the Pisarenko curve based on a two-band model, which considers the contributions from two valence bands.

values of all SnTe films are determined mainly by σ. In the SnTe films grown at a fixed Te/Sn ratio of 6/1, increasing T_{sub} leads to a dramatically decreased p, which reduces the σ and *PF*. In SnTe films grown at fixed T_{sub} of 593 or 633 K, higher *PF*s are obtained in films with lower Te/Sn ratio, which have improved μ and σ. The SnTe film grown at a T_{sub} of 553 K and a Te/Sn ratio of 6/1, possesses a high *PF* of 1.01 mW m^{-1} K^{-2} at room temperature because of the high p of 8.31 × 10^{20} cm^{-3} and the moderate μ of approximately 28.8 cm^2 V^{-1} s^{-1}. The SnTe film grown at a T_{sub} of 593 K and a Te/Sn ratio of 2/1 yields the highest *PF* of 1.73 mW m^{-1} K^{-2} at 673 K, resulting from the excellent μ and the moderate p. It is noteworthy that, unlike the prominent change in σ, the change in S is relatively minor for different SnTe films. This feature differs from bulk SnTe, in which S strongly depends upon p.[30,53] Nevertheless, the best *PF* achieved in our SnTe films is inferior to that in SnTe bulks, which is mainly due to the relatively low μ.[30,54]

To further clarify the transport feature of the grown SnTe films, we show in Figure 7 plots of μ, S, and *PF* as functions of p. The data from SnTe bulks are also included for comparison. The μ of SnTe films is lower than that of reported SnTe bulks. For example, SnTe bulks could achieve a μ of approximately 200 cm^2 V^{-1} s^{-1} at $p \approx 2.0 \times 10^{20}$ cm^{-3}, which is approximately 150% larger than the μ value in films that had an identical p.[30,54,55] The lower μ in SnTe films is most likely due to the reference-outlined downward band bending in the Te-terminated surface[56] and the high-density spiral grain boundaries in atomically grown MBE films.[57] The Pisarenko plot calculated with the two valence bands model covers three stages, with p increasing up to 2 × 10^{21} cm^{-3}. The experimentally obtained S–p relation in our SnTe films follows the general trend of the Pisarenko curve but with higher S values than the calculations. Moreover, the S of SnTe films is higher than that of bulks with similar p. The strikingly enhanced S and the reduced μ may suggest the existence of an energy filtering effect in SnTe films.[58] Consequently, the room-temperature *PF*s of our SnTe films are comparable to the values in most SnTe bulks, as shown in Figure 7c.[26,29−31,54,55,59,60]

The above analysis indicates that the p of SnTe films can be tuned over a wide range of 1.82–8.69 × 10^{20} cm^{-3} by manipulating the native atomic defects of the positively charged V_{Sn} and negatively charged Sn_i. The MBE process parameters, especially T_{sub}, play vital roles in regulating atomic defects and therefore the p, μ, and S values of SnTe (111) films. Thus, the *PF*s can be enhanced by rationally designing the growth conditions to control the atomic defects.

4. CONCLUSION

In this study, SnTe (111) films with high crystallinity were successfully grown by MBE at various T_{sub} and Te/Sn ratios to examine native atomic defects and their associated effects on electrical transport properties. The in situ STM topographies have clarified that the positively charged V_{Sn} and Sn_{Te}, as well as the negatively charged V_{Te} and Sn_i, are native atomic defects in SnTe. And, V_{Sn} and Sn_i are the dominant defects that govern the electronic transport properties of SnTe films, as further confirmed by DFT simulations. In general, high T_{sub} greatly reduces the density of V_{Sn} and the p due to a decreased Te content in the film. In addition, a high T_{sub} and a low Te/Sn ratio simultaneously increase the densities of V_{Sn} and Sn_i, which are driven by excess Sn and increased thermal energy, leading to fluctuations in the p. The variations in p in SnTe films grown at various MBE parameters are consistent with the E_F determined by ARPES. As T_{sub} increases and Te/Sn ratio decreases, the p of SnTe films is dramatically reduced from 8.69 × 10^{20} cm^{-3} to 1.82 × 10^{20} cm^{-3}. Furthermore, μ is significantly enhanced as T_{sub} increases, originating from the improved crystallinity of the films. Maintaining a high T_{sub} and a low Te/Sn ratio are beneficial for optimizing p and μ, and hence the *PF*. As a result, the SnTe film grown at a T_{sub} of 593 K and a Te/Sn ratio of 2/1 obtains the highest *PF* of 1.73 mW m^{-1} K^{-2} at 673 K. This work provides direct experimental evidence on the manipulation of native atomic defects in SnTe, which is expected to enlighten the enhancement of electronic transport properties in SnTe-based bulks and films.

■ ASSOCIATED CONTENT

Supporting Information

The Supporting Information is available free of charge at https://pubs.acs.org/doi/10.1021/acsami.1c15447.

STM atomic defect structure for SnTe films under different bias voltages; ARPES electronic band structures along the $\bar{\Gamma}$–$\bar{M}$ and $\bar{\Gamma}$–$\bar{K}$ directions over a wide momentum range; ARPES electronic band structures for SnTe (111) films grown at T_{sub} = 593 K and various Te/Sn ratios; temperature dependence of electrical transport properties of SnTe (111) films in a heating/cooling cycle (PDF)

■ AUTHOR INFORMATION

Corresponding Authors

Wei Liu − *State Key Laboratory of Advanced Technology for Materials Synthesis and Processing, Wuhan University of*

https://doi.org/10.1021/acsami.1c15447
ACS Appl. Mater. Interfaces XXXX, XXX, XXX−XXX

Technology, Wuhan 430070, China; orcid.org/0000-0002-3245-7270; Email: w.liu@whut.edu.cn

Xinfeng Tang − *State Key Laboratory of Advanced Technology for Materials Synthesis and Processing, Wuhan University of Technology, Wuhan 430070, China;* orcid.org/0000-0001-7555-919X; Email: tangxf@whut.edu.cn

Authors

Fuqiang Hua − *State Key Laboratory of Advanced Technology for Materials Synthesis and Processing, Wuhan University of Technology, Wuhan 430070, China; International School of Materials Science and Engineering, Wuhan University of Technology, Wuhan 430070, China;* orcid.org/0000-0003-0416-1517

Pengfei Lv − *School of Physics and Technology, Wuhan University, Wuhan 430070, China*

Min Hong − *Centre for Future Materials, University of Southern Queensland, Springfield, Queensland 4300, Australia*

Sen Xie − *State Key Laboratory of Advanced Technology for Materials Synthesis and Processing, Wuhan University of Technology, Wuhan 430070, China; International School of Materials Science and Engineering, Wuhan University of Technology, Wuhan 430070, China*

Min Zhang − *State Key Laboratory of Advanced Technology for Materials Synthesis and Processing, Wuhan University of Technology, Wuhan 430070, China*

Cheng Zhang − *State Key Laboratory of Advanced Technology for Materials Synthesis and Processing, Wuhan University of Technology, Wuhan 430070, China;* orcid.org/0000-0003-0450-4321

Wei Wang − *State Key Laboratory of Advanced Technology for Materials Synthesis and Processing, Wuhan University of Technology, Wuhan 430070, China*

Zhaohui Wang − *State Key Laboratory of Advanced Technology for Materials Synthesis and Processing, Wuhan University of Technology, Wuhan 430070, China; International School of Materials Science and Engineering, Wuhan University of Technology, Wuhan 430070, China*

Yong Liu − *School of Physics and Technology, and the Key Laboratory of Artificial Micro/Nano structures of Ministry of Education, Wuhan University, Wuhan 430072, China*

Yonggao Yan − *State Key Laboratory of Advanced Technology for Materials Synthesis and Processing, Wuhan University of Technology, Wuhan 430070, China*

Shengjun Yuan − *School of Physics and Technology, Wuhan University, Wuhan 430070, China;* orcid.org/0000-0001-6208-1502

Complete contact information is available at: https://pubs.acs.org/10.1021/acsami.1c15447

Author Contributions

X.T. and W.L. supervised this project. X.T., W.L., M.H. and F.H. conceived the experiments and wrote the draft of the manuscript. F.H., M.Z., and Z.W. performed the MBE growth of films. F.H., C.Z., and W.W. performed the STM measurements. F.H. and S.X. carried out the ARPES measurements. P.L., M.H., and S.Y. carried out theoretical calculations. F.H., Y.L., and Y.Y. performed the HRXRD measurements.

Author Contributions

†F.H. and P.L. contributed equally to this paper

Notes

The authors declare no competing financial interest.

■ ACKNOWLEDGMENTS

The work was supported by the Natural Science Foundation of China (Grant 91963120, 51632006, 51521001 and 12074291), National Key Research and Development Program of China (Grants 2019YFA0704900, 2018YFA0305800, and 2018YFB0703600), and Wuhan Frontier Project on Applied Research Foundation (Grant 2019010701011405). Numerical calculations presented in this paper have been performed on a supercomputing system in the Supercomputing Center of Wuhan University.

■ REFERENCES

(1) Julian Goldsmid, H. *Introduction to Thermoelectricity*; Springer: Berlin, 2010; Vol. *121*.

(2) Champier, D. Thermoelectric Generators: A Review of Applications. *Energy Convers. Manage.* **2017**, *140*, 167−181.

(3) Zhang, Y. Thermoelectric Advances to Capture Waste Heat in Automobiles. *ACS Energy Letters* **2018**, *3* (7), 1523−1524.

(4) Nozariasbmarz, A.; Suarez, F.; Dycus, J. H.; Cabral, M. J.; LeBeau, J. M.; Öztürk, M. C.; Vashaee, D. Thermoelectric Generators for Wearable Body Heat Harvesting: Material and Device Concurrent Optimization. *Nano Energy* **2020**, *67*, 104265.

(5) Chowdhury, I.; Prasher, R.; Lofgreen, K.; Chrysler, G.; Narasimhan, S.; Mahajan, R.; Koester, D.; Alley, R.; Venkatasubramanian, R. On-chip Cooling by Superlattice-based Thin-film Thermoelectrics. *Nat. Nanotechnol.* **2009**, *4* (4), 235−238.

(6) Snyder, G. J.; Toberer, E. S. Complex Thermoelectric Materials. *Nat. Mater.* **2008**, *7* (2), 105−114.

(7) Li, W.; Wu, Y.; Lin, S.; Chen, Z.; Li, J.; Zhang, X.; Zheng, L.; Pei, Y. Advances in Environment-Friendly SnTe Thermoelectrics. *ACS Energy Letters* **2017**, *2* (10), 2349−2355.

(8) Wang, L.; Tan, X.; Liu, G.; Xu, J.; Shao, H.; Yu, B.; Jiang, H.; Yue, S.; Jiang, J. Manipulating Band Convergence and Resonant State in Thermoelectric Material SnTe by Mn-In Codoping. *ACS Energy Letters* **2017**, *2* (5), 1203−1207.

(9) Roychowdhury, S.; Biswas, R. K.; Dutta, M.; Pati, S. K.; Biswas, K. Phonon Localization and Entropy-Driven Point Defects Lead to Ultralow Thermal Conductivity and Enhanced Thermoelectric Performance in $(SnTe)_{1-2x}(SnSe)_x(SnS)_x$. *ACS Energy Letters* **2019**, *4* (7), 1658−1662.

(10) Li, W.; Zheng, L.; Ge, B.; Lin, S.; Zhang, X.; Chen, Z.; Chang, Y.; Pei, Y. Promoting SnTe as an Eco-Friendly Solution for P-PbTe Thermoelectric via Band Convergence and Interstitial Defects. *Adv. Mater.* **2017**, *29* (17), 1605887.

(11) Jiang, Q.; Hu, H.; Yang, J.; Xin, J.; Li, S.; Viola, G.; Yan, H. High Thermoelectric Performance in SnTe Nanocomposites with All-Scale Hierarchical Structures. *ACS Appl. Mater. Interfaces* **2020**, *12* (20), 23102−23109.

(12) Tang, J.; Gao, B.; Lin, S.; Li, J.; Chen, Z.; Xiong, F.; Li, W.; Chen, Y.; Pei, Y. Manipulation of Band Structure and Interstitial Defects for Improving Thermoelectric SnTe. *Adv. Funct. Mater.* **2018**, *28* (34), 1803586.

(13) Li, W.; Chen, Z.; Lin, S.; Chang, Y.; Ge, B.; Chen, Y.; Pei, Y. Band and Scattering Tuning for High Performance Thermoelectric $Sn_{1-x}Mn_xTe$ Alloys. *Journal of Materiomics* **2015**, *1* (4), 307−315.

(14) Tan, G.; Shi, F.; Hao, S.; Chi, H.; Zhao, L. D.; Uher, C.; Wolverton, C.; Dravid, V. P.; Kanatzidis, M. G. Codoping in SnTe: Enhancement of Thermoelectric Performance through Synergy of Resonance Levels and Band Convergence. *J. Am. Chem. Soc.* **2015**, *137* (15), 5100−5112.

(15) Tan, G.; Shi, F.; Doak, J. W.; Sun, H.; Zhao, L.; Wang, P.; Uher, C.; Wolverton, C.; Dravid, V. P.; Kanatzidis, M. G. Extraordinary Role of Hg in Enhancing the Thermoelectric Performance of P-type SnTe. *Energy Environ. Sci.* **2015**, *8* (1), 267−277.

(16) Banik, A.; Shenoy, U. S.; Anand, S.; Waghmare, U. V.; Biswas, K. Mg Alloying in SnTe Facilitates Valence Band Convergence and Optimizes Thermoelectric Properties. *Chem. Mater.* **2015**, *27* (2), 581−587.
(17) Zhang, Q.; Liao, B.; Lan, Y.; Lukas, K.; Liu, W.; Esfarjani, K.; Opeil, C.; Broido, D.; Chen, G.; Ren, Z. High Thermoelectric Performance by Resonant Dopant Indium in Nanostructured SnTe. *Proc. Natl. Acad. Sci. U. S. A.* **2013**, *110* (33), 13261−13266.
(18) Li, D.; Ming, H. W.; Li, J. M.; Zhang, J.; Qin, X. Y.; Xu, W. High Thermoelectric Performance of SnTe via In Doping and $Cu_{1.75}Se$ Nanostructuring Approach. *ACS Applied Energy Materials* **2019**, *2* (12), 8966−8973.
(19) Zheng, L.; Li, W.; Lin, S.; Li, J.; Chen, Z.; Pei, Y. Interstitial Defects Improving Thermoelectric SnTe in Addition to Band Convergence. *ACS Energy Letters* **2017**, *2* (3), 563−568.
(20) Xin, J.; Li, S.; Yang, J.; Basit, A.; Long, Q.; Li, S.; Jiang, Q.; Xu, T.; Xiao, B. Tactfully Decoupling Interdependent Electrical Parameters via Interstitial Defects for SnTe Thermoelectrics. *Nano Energy* **2020**, *67*, 104292.
(21) Guo, F.; Cui, B.; Liu, Y.; Meng, X.; Cao, J.; Zhang, Y.; He, R.; Liu, W.; Wu, H.; Pennycook, S. J.; Cai, W.; Sui, J. Thermoelectric SnTe with Band Convergence, Dense Dislocations, and Interstitials through Sn Self-Compensation and Mn Alloying. *Small* **2018**, *14* (37), 1802615.
(22) Hong, M.; Wang, Y.; Xu, S.; Shi, X.; Chen, L.; Zou, J.; Chen, Z.-G. Nanoscale Pores Plus Precipitates Rendering High-performance Thermoelectric $SnTe_{1-x}Se_x$ with Refined Band Structures. *Nano Energy* **2019**, *60*, 1−7.
(23) Pei, Y.; Zheng, L.; Li, W.; Lin, S.; Chen, Z.; Wang, Y.; Xu, X.; Yu, H.; Chen, Y.; Ge, B. Interstitial Point Defect Scattering Contributing to High Thermoelectric Performance in SnTe. *Advanced Electronic Materials* **2016**, *2* (6), 1600019.
(24) Zhao, L. D.; Zhang, X.; Wu, H.; Tan, G.; Pei, Y.; Xiao, Y.; Chang, C.; Wu, D.; Chi, H.; Zheng, L.; Gong, S.; Uher, C.; He, J.; Kanatzidis, M. G. Enhanced Thermoelectric Properties in the Counter-Doped SnTe System with Strained Endotaxial SrTe. *J. Am. Chem. Soc.* **2016**, *138* (7), 2366−73.
(25) Wang, N.; West, D.; Liu, J.; Li, J.; Yan, Q.; Gu, B.-L.; Zhang, S. B.; Duan, W. Microscopic Origin of the P-Type Conductivity of the Topological Crystalline Insulator SnTe and the Effect of Pb Alloying. *Phys. Rev. B: Condens. Matter Mater. Phys.* **2014**, *89* (4), 045142.
(26) Zhou, Z.; Yang, J.; Jiang, Q.; Luo, Y.; Zhang, D.; Ren, Y.; He, X.; Xin, J. Multiple Effects of Bi Doping in Enhancing the Thermoelectric Properties of SnTe. *J. Mater. Chem. A* **2016**, *4* (34), 13171−13175.
(27) Zhou, Z.; Yang, J.; Jiang, Q.; Lin, X.; Xin, J.; Basit, A.; Hou, J.; Sun, B. Enhanced Thermoelectric Performance of SnTe: High Efficient Cation-anion Co-doping, Hierarchical Microstructure and Electro-acoustic Decoupling. *Nano Energy* **2018**, *47*, 81−88.
(28) Kihoi, S. K.; Shenoy, U. S.; Bhat, D. K.; Lee, H. S. Complementary Effect of Co-doping Aliovalent Elements Bi and Sb in Self-compensated SnTe-based Thermoelectric Materials. *J. Mater. Chem. C* **2021**, *9*, 9922−9931.
(29) Zhou, M.; Gibbs, Z. M.; Wang, H.; Han, Y.; Xin, C.; Li, L.; Snyder, G. J. Optimization of Thermoelectric Efficiency in SnTe: the Case for the Light Band. *Phys. Chem. Chem. Phys.* **2014**, *16* (38), 20741−20748.
(30) Tan, G.; Zhao, L. D.; Shi, F.; Doak, J. W.; Lo, S. H.; Sun, H.; Wolverton, C.; Dravid, V. P.; Uher, C.; Kanatzidis, M. G. High Thermoelectric Performance of P-type SnTe via a Synergistic Band Engineering and Nanostructuring Approach. *J. Am. Chem. Soc.* **2014**, *136* (19), 7006−7017.
(31) Banik, A.; Biswas, K. AgI Alloying in SnTe Boosts the Thermoelectric Performance via Simultaneous Valence Band Convergence and Carrier Concentration Optimization. *J. Solid State Chem.* **2016**, *242*, 43−49.
(32) Li, S.; Yang, J.; Xin, J.; Jiang, Q.; Zhou, Z.; Hu, H.; Sun, B.; Basit, A.; Li, X. Tailoring the Carrier and Phonon Scattering to Enhanced Thermoelectric Performance of SnTe by Cation-Anion Codoping with Eco-Benign CaI_2. *ACS Applied Energy Materials* **2019**, *2* (3), 1997−2003.
(33) Huo, H.; Wang, Y.; Xi, L.; Yang, J.; Zhang, W. The Variation of Intrinsic Defects in XTe (X = Ge, Sn, and Pb) Induced by the Energy Positions of Valence Band Maxima. *J. Mater. Chem. C* **2021**, *9* (17), 5765−5770.
(34) Zhang, L.; Wang, J.; Cheng, Z.; Sun, Q.; Li, Z.; Dou, S. Lead-Free SnTe-Based Thermoelectrics: Enhancement of Thermoelectric Performance by Doping with Gd/Ag. *J. Mater. Chem. A* **2016**, *4* (20), 7936−7942.
(35) Netsou, A. M.; Muzychenko, D. A.; Dausy, H.; Chen, T.; Song, F.; Schouteden, K.; Van Bael, M. J.; Van Haesendonck, C. Identifying Native Point Defects in the Topological Insulator Bi_2Te_3. *ACS Nano* **2020**, *14* (10), 13172−13179.
(36) Zhang, M.; Liu, W.; Zhang, C.; Xie, S.; Li, Z.; Hua, F.; Luo, J.; Wang, Z.; Wang, W.; Yan, F.; Cao, Y.; Liu, Y.; Wang, Z.; Uher, C.; Tang, X. Identifying the Manipulation of Individual Atomic-Scale Defects for Boosting Thermoelectric Performances in Artificially Controlled Bi_2Te_3 Films. *ACS Nano* **2021**, *15* (3), 5706−5714.
(37) Zhang, D.; Baek, H.; Ha, J.; Zhang, T.; Wyrick, J.; Davydov, A. V.; Kuk, Y.; Stroscio, J. A. Quasiparticle Scattering from Topological Crystalline Insulator SnTe (001) Surface States. *Phys. Rev. B: Condens. Matter Mater. Phys.* **2014**, *89* (24), 245445.
(38) Schreyeck, S.; Brunner, K.; Molenkamp, L. W.; Karczewski, G.; Schmitt, M.; Sessi, P.; Vogt, M.; Wilfert, S.; Odobesko, A. B.; Bode, M. Breaking Crystalline Symmetry of Epitaxial SnTe Films by Strain. *Physical Review Materials* **2019**, *3* (2), 024203.
(39) Giannozzi, P.; Baroni, S.; Bonini, N.; Calandra, M.; Car, R.; Cavazzoni, C.; Ceresoli, D.; Chiarotti, G. L.; Cococcioni, M.; Dabo, I.; Dal Corso, A.; de Gironcoli, S.; Fabris, S.; Fratesi, G.; Gebauer, R.; Gerstmann, U.; Gougoussis, C.; Kokalj, A.; Lazzeri, M.; Martin-Samos, L.; Marzari, N.; Mauri, F.; Mazzarello, R.; Paolini, S.; Pasquarello, A.; Paulatto, L.; Sbraccia, C.; Scandolo, S.; Sclauzero, G.; Seitsonen, A. P.; Smogunov, A.; Umari, P.; Wentzcovitch, R. M. QUANTUM ESPRESSO: A Modular and Open-source Software Project for Quantum Simulations of Materials. *J. Phys.: Condens. Matter* **2009**, *21* (39), 395502.
(40) Perdew, J. P.; Burke, K.; Ernzerhof, M. Ernzerhof, Generalized Gradient Approximation Made Simple. *Phys. Rev. Lett.* **1996**, *77* (18), 3865.
(41) Van de Walle, C. G.; Neugebauer, J. First-principles Calculations for Defects and Impurities: Applications to III-Nitrides. *J. Appl. Phys.* **2004**, *95* (8), 3851−3879.
(42) Blochl, P. E. Projector Augmented-wave Method. *Phys. Rev. B: Condens. Matter Mater. Phys.* **1994**, *50* (24), 17953−17979.
(43) Kresse, G.; Furthmuller, J. Efficient Iterative Schemes for Ab initio Total-Energy Calculations Using A Plane-Wave Basis Set. *Phys. Rev. B: Condens. Matter Mater. Phys.* **1996**, *54* (16), 11169.
(44) Monkhorst, H. J.; Pack, J. D. Special Points for Brillouin-zone Integrations. *Phys. Rev. B* **1976**, *13* (12), 5188−5192.
(45) Tersoff, J.; Hamann, D. R. Theory and Application for the Scanning Tunneling Microscope. *Phys. Rev. Lett.* **1983**, *50* (25), 1998−2001.
(46) Tersoff, J.; Hamann, D. R. Theory of the Scanning Tunneling Microscope. *Phys. Rev. B: Condens. Matter Mater. Phys.* **1985**, *31* (2), 805−813.
(47) Taskin, A. A.; Yang, F.; Sasaki, S.; Segawa, K.; Ando, Y. Topological Surface Transport in Epitaxial SnTe Thin Films Grown on Bi_2Te_3. *Phys. Rev. B: Condens. Matter Mater. Phys.* **2014**, *89* (12), 121302.
(48) Zhang, M.; Liu, W.; Zhang, C.; Qiu, J.; Xie, S.; Hua, F.; Cao, Y.; Li, Z.; Xie, H.; Uher, C.; Tang, X. Thickness-Dependent Electronic Transport Induced by in Situ Transformation of Point Defects in MBE-Grown Bi_2Te_3 Thin Films. *Appl. Phys. Lett.* **2020**, *117* (15), 153902.
(49) Levy, I.; Garcia, T. A.; Shafique, S.; Tamargo, M. C. Reduced Twinning and Surface Roughness of Bi_2Se_3 and Bi_2Te_3 Layers Grown by Molecular Beam Epitaxy on Sapphire Substrates. *J. Vac. Sci.*

https://doi.org/10.1021/acsami.1c15447
ACS Appl. Mater. Interfaces XXXX, XXX, XXX−XXX

Technol., B: Nanotechnol. Microelectron.: Mater., Process., Meas., Phenom. **2018**, *36* (2), 02D107.
(50) Xu, W.; Yang, H.; Liu, C.; Zhang, Z.; Chen, C.; Ye, Z.; Lu, Z.; Wang, X.; Gao, J.; Chen, J.; Xie, Z.; Miao, L. Optimized Electronic Bands and Ultralow Lattice Thermal Conductivity in Ag and Y Codoped SnTe. *ACS Appl. Mater. Interfaces* **2021**, *13* (28), 32876−32885.
(51) Wang, J.; Liu, J.; Xu, Y.; Wu, J.; Gu, B.; Duan, W. Structural Stability and Topological Surface States of the SnTe (111) Surface. *Phys. Rev. B: Condens. Matter Mater. Phys.* **2014**, *89* (12), 125308.
(52) Tanaka, Y.; Shoman, T.; Nakayama, K.; Souma, S.; Sato, T.; Takahashi, T.; Novak, M.; Segawa, K.; Ando, Y. Two types of Dirac-cone Surface States on the (111) Surface of the Topological Crystalline Insulator SnTe. *Phys. Rev. B: Condens. Matter Mater. Phys.* **2013**, *88* (23), 235126.
(53) Brebrick, R. F.; Strauss, A. J. Anomalous Thermoelectric Power as Evidence for Two-Valence Bands in SnTe. *Phys. Rev.* **1963**, *131* (1), 104−110.
(54) Lee, M. H.; Byeon, D.; Rhyee, J.; Ryu, B. Defect Chemistry and Enhancement of Thermoelectric Performance in Ag-doped $Sn_{1+\delta-x}Ag_xTe$. *J. Mater. Chem. A* **2017**, *5* (5), 2235−2242.
(55) Brebrick, R. F. Deviations from Stoichiometry and Electrical Properties in SnTe. *J. Phys. Chem. Solids* **1963**, *24* (1), 27−36.
(56) Zhang, Z.; Yates, J. T., Jr. Band Bending in Semiconductors: Chemical and Physical Consequences at Surfaces and Interfaces. *Chem. Rev.* **2012**, *112* (10), 5520−5551.
(57) Springholz, G.; Ueta, A. Y.; Frank, N.; Bauer, G. Spiral Growth and Threading Dislocations for Molecular Beam Epitaxy of PbTe on BaF_2 (111) Studied by Scanning Tunneling Microscopy. *Appl. Phys. Lett.* **1996**, *69* (19), 2822−2824.
(58) Gayner, C.; Amouyal, Y. Energy Filtering of Charge Carriers: Current Trends, Challenges, and Prospects for Thermoelectric Materials. *Adv. Funct. Mater.* **2020**, *30* (18), 1901789.
(59) Li, S.; Xin, J.; Li, W.; Tao, Y.; Xu, T.; Xiao, B.; Luo, Y.; Jiang, Q.; Yang, J. Enhanced Thermoelectric Performance of Orientated and Defected SnTe. *J. Alloys Compd.* **2021**, *858*, 157634.
(60) Xu, S.; Zhu, W.; Zhao, H.; Xu, L.; Sheng, P.; Zhao, G.; Deng, Y. Enhanced Thermoelectric Performance of SnTe Thin Film through Designing Oriented Nanopillar Structure. *J. Alloys Compd.* **2018**, *737*, 167−173.

https://doi.org/10.1021/acsami.1c15447
ACS Appl. Mater. Interfaces XXXX, XXX, XXX−XXX